NANO LETTERS
Letter
Cite This: *Nano Lett.* 2019, 19, 1512−1519
pubs.acs.org/NanoLett

Conversion of Metal−Organic Cage to Ligand-Free Ultrasmall Noble Metal Nanocluster Catalysts Confined within Mesoporous Silica Nanoparticle Supports

Wei Zhu,[†] Achraf Noureddine,[†] Jane Y. Howe,[‡] Jimin Guo,[†] and C. Jeffrey Brinker*[,†,§]

[†]Center for Micro-Engineered Materials and the Department of Chemical and Biological Engineering, The University of New Mexico, Albuquerque, New Mexico 87131, United States

[‡]Nanotechnology Systems Division, Hitachi High-Technologies America Inc., 22610 Gateway Center Drive #100, Clarksburg, Maryland 20871, United States

[§]Advanced Materials Laboratory, Sandia National Laboratories, Albuquerque, New Mexico 87185, United States

Supporting Information

ABSTRACT: Supported ultrasmall noble metal nanocluster-based (UNMN-based) catalysts are one of the most important classes of solid materials for heterogeneous catalysis. In this work, we present a novel strategy for the controlled synthesis of ligand-free UNMN nanocatalysts based on in situ reduction of a palladium-based (Pd-based) metal−organic cage (MOC) confined within monosized, thiol-modified mesoporous silica nanoparticle (MSN) supports. By taking advantage of the high mutual solubility of MOCs and MSNs in DMSO and the strong interactions between the thiol-modified MSN pore wall and MOC surface, a good dispersion of MOC molecules was achieved throughout the MSN support. The close correspondence of the MSN pore diameter (ca. 5.0 nm) with the diameter of the MOC (ca. 4.0 nm) confines MOC packing to approximately a monolayer. Based on this spatial constraint and electrostatic binding of the MOC to the thiol-modified MSN pore surface, in situ MOC reduction followed by metal atom diffusion, coalescence, and anchoring on the active sites resulted in ligand-free Pd-based UNMNs of approximately 0.9 ± 0.2 nm in diameter decorating the MSN pore surfaces. Control experiments of the reduction of a conventional palladium source or the reduction of free, unconstrained cages in solution under the same conditions only produced large metal nanocrystals (NP, >2 nm), confirming the importance of confined reduction to achieve a highly catalytically active surface. In light of this strategy, two catalytic experiments including the reaction of 4-nitrophenol to 4-aminophenol and the Suzuki C−C coupling reaction show superior catalytic activity of the engineered MSN-supported UNMN nanocatalysts compared to their free form and state of the art commercial catalysts. We believe that our new strategy will open new avenues for artificially designed UNMN-inspired nanoarchitectures for wide applications.

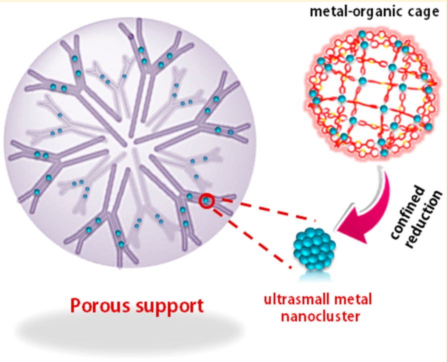

KEYWORDS: *Ultrasmall noble metal nanocluster, metal−organic cage, mesoporous silica nanoparticle, confined space, heterogeneous catalysis*

Due to high catalytic activity, selective reactivity, and recyclability, noble metal nanoparticles (NPs), especially platinum (Pt) and palladium (Pd), supported on porous carriers with high surface area have been extensively studied for heterogeneous catalytic reactions.[1−4] Up to now, numerous theoretical and experimental studies have proven the size-dependent catalytic activities of noble metal nanoparticles.[5−7] Especially, for ultrasmall noble metal nanoclusters (UNMNs) that consist of several to hundreds of metal atoms, even a one-atom difference can cause significant transitions in the catalytic activity or selectivity due to electronic and geometric configuration variations.[8−11] Examples include the significant different catalytic activities in Ir_4 and Ir_6 nanoclusters (NCs) for hydrocarbon hydrogenation reactions,[12] the strong size variation in CO oxidation activity for Pd NCs,[13] and the atomic-specific catalytic activity in Pt NCs,[14] etc. These amazing size-/atom-number-dependent properties demand the construction of advanced UNMN-based nanoarchitectures/nanocatalysts for various catalytic applications. Currently, direct reduction of metal sources in solid porous supports such as mesoporous silica nanoparticles (MSNs) or metal−organic frameworks have been used extensively for supported UNMN catalyst synthesis; however, these synthetic methods often exhibit lack of size control and result in broad size distribution.[15,16] Alternatively, sequential two-step syntheses involving the presynthesis of UNMNs in solution phase under

Received: October 14, 2018
Revised: January 23, 2019
Published: February 4, 2019

DOI: 10.1021/acs.nanolett.8b04121

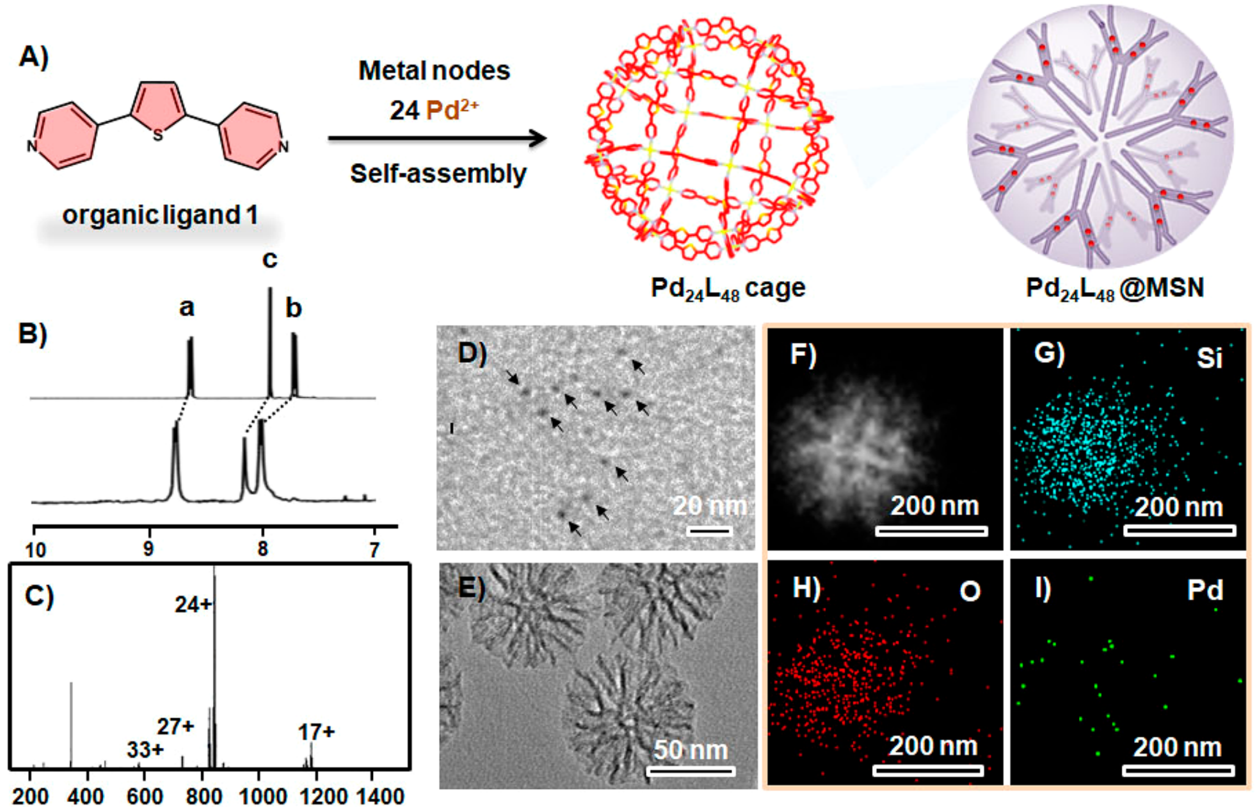

Figure 1. (A) Self-assembly of $Pd_{24}L_{48}$ cage and the related loading and packing in 3D-dendritic MSN. (B) ^1H NMR spectra (300 MHz, DMSO-d_6) of organic ligand 1 and $Pd_{24}L_{48}$ cage. ESI-MS (C) and TEM image (D) of $Pd_{24}L_{48}$ cage. TEM image (E) and dark-field STEM image (F) of the synthesized 3D-dendritic MSN. (G−I) EDX elemental mapping of $Pd_{24}L_{48}$ cage loaded in 3D-dendritic MSN.

the protection of excess capping agents such as phosphine, thiol, PVP, etc., or confined reduction within various templates such as dendrimers and micelles, followed by transfer onto solid supports, represent powerful approaches for the fabrication of supported UNMN catalysts with good control of NC size and nanostructure.[17] However, the surface capping agents block the catalytic sites, and thus decrease catalytic activity and selectivity, and potential metal NC leakage or low loading efficiency, in some cases, limit further applications.[18] Additional strategies such as the in situ growth of UNMN on carbon supports via a "soft intruding" method have also been reported.[19] Nevertheless, the development of a facile and general synthetic method for the controlled synthesis of ligand-free supported UNMN nanocatalysts remains highly desirable.

Metal−organic cages (MOCs), discrete molecular cages with well-defined structures and high symmetries constructed through the coordination of organic ligands and metal ions, have attracted increasing attention for catalysis, molecular recognition, and sensing.[20−26] Careful selection of the bridging ligands and metal ions permits the rational control of a well-confined inner space, gated pores, nanoscale windows, and especially the strict control of the number of metal centers.[27−31] More importantly, various guest molecules, including polyoxometalate and metal ion clusters, can also be loaded into the host cage in a controlled fashion.[32−34] These distinctive features make MOC an excellent candidate for the synthesis of supported single or hybrid UNMN-based catalysts. In this field, the Fujita group reported the controlled synthesis of UNMNs within hollow silica NPs.[35] Upon sol−gel condensation of silica around the cage, and subsequent calcination and reduction, Pd_{12} NC-containing hollow silica NPs were efficiently prepared. Nevertheless, due to the encapsulation of UNMNs within nonporous silica shells, the related catalytic activity would presumably be hindered. Up to now, the synthesis of supported UNMN nanocatalysts via MOC is still very limited, and consequently the investigation and assessment of new functions of the novel MOC-based UNMNs/nanoarchitectures is also less well-studied but of potentially high interest.

Herein we develop a novel strategy for the controlled synthesis of ligand-free UNMN nanocatalysts based on an in situ reduction of MOC molecules confined within a thiol-modified mesoporous silica nanoparticle support (Figure 1A). The key point is the size correspondence between the silica nanopore (ca. 5.0 nm) and MOC (ca. 4.0 nm). On one hand, by taking advantage of the good solubility of MOC in solution and the strong electrostatic interaction between the positive MOC and negative mesoporous silica wall, the formed organic−inorganic hybrid composite, termed as mesoporous silica-confined MOC (MOC@MSN), displays a good dispersion of MOC within the MSN support. On the other hand, due to size constraints imposed by the MSN pore walls, only a single monolayer or sub-monolayer of MOC is strictly allowed along an entire silica nanopore, where upon MOC reduction, and subsequent metal atom diffusion, coalescence, and anchoring on surface thiols, the reduced, "free" metal atoms from MOC finally form a ligand-free UNMN-decorated MSN pore surface with controlled UNMN size of ca. 0.9 ± 0.2 nm. Control experiments of the reduction of a conventional palladium source or the reduction of free, unconstrained cages in solution under the same conditions only produced large metal NPs, confirming the importance of confined reduction.

DOI: 10.1021/acs.nanolett.8b04121
Nano Lett. 2019, 19, 1512−1519

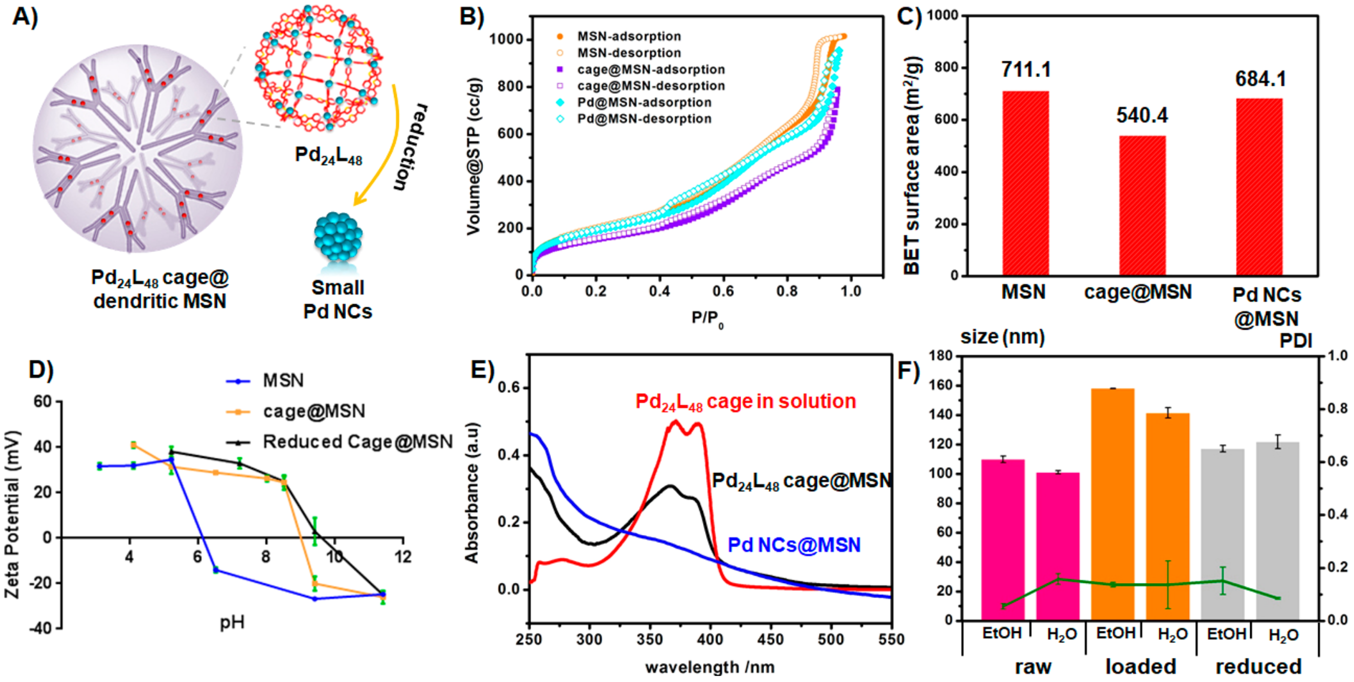

Figure 2. (A) Schematic illustration of the conversion of Pd$_{24}$L$_{48}$ cage into ultrasmall Pd NCs in dendritic MSN. N$_2$ sorption isotherms (B) for Pd$_{24}$L$_{48}$ cage, Pd$_{24}$L$_{48}$ cage@MSN, and Pd NCs@MSN, and the related BET surface area (C). (D) ζ potential of MSN, Pd$_{24}$L$_{48}$ cage@MSN, and reduced cage@MSN at different pHs. (E) UV−vis spectra of Pd$_{24}$L$_{48}$ cage, Pd$_{24}$L$_{48}$ cage@MSN, and Pd NCs@MSN in aqueous solution. (F) Hydrodynamic size and the related PDI of bare MSNs, Pd$_{24}$L$_{48}$ cage@MSN, and Pd NCs@ MSN suspended in ethanol or water.

Importantly, the fast reduction of 4-nitrophenol to 4-aminophenol and the good catalytic performance in the Suzuki C−C coupling reaction by using Pd NCs@MSN as heterogeneous catalysts highlight the successful activity of Pd NCs confined in MSN. We believe that our new strategy would not only bridge the field of MSN-based materials with theoretically infinite MOC species but also open new avenues for artificially designed UNMN-inspired nanoarchitectures with target functionalities.

Results and Discussion. A four-step procedure was employed to prepare the UNMN-functionalized MSN. For easier structural characterization of the obtained metal NCs, a large MOC, Pd$_{24}$L$_{48}$ (diameter: ca. 4.0 nm), which was first reported by Fujita's group,[27] was used in our case for demonstration. First, ligand 1 (Figure 1A) was synthesized in one step based on the Suzuki−Miyaura reaction between 2,5-dibromo-thiophene and 4-pyridylboronic acid pinacol ester. To synthesize the Pd$_{24}$L$_{48}$ cage, ligand 1 (0.1 mmol) and Pd(NO$_3$)$_2$ (50 μmol) were heated in dimethyl sulfoxide (DMSO) (7.0 mL) at 70 °C for 17 h. Then an excess amount of mixed solution of ethyl acetate and diethyl ether (1:1 in volume) was added to promote the precipitation of the cage. After washing several times with ethyl acetate and centrifugation, the obtained Pd$_{24}$L$_{48}$ cage was redissolved in DMSO solution for subsequent loading (see detailed preparation procedures in the Supporting Information). Second, monosized 3D-dendritic MSNs with pore size of ca. 5.0 nm were prepared through a biphasic reaction and functionalized with a thiol-bearing silane (3-(4-pyridylethyl) thiopropyltrimethoxysilane) by a delayed condensation procedure.[36,37] The thiol groups serve as anchoring sites for clusters during MOC reduction. Third, the obtained template-free dendritic MSNs were dispersed in the Pd$_{24}$L$_{48}$ cage solution and incubated overnight for cage loading. Finally, after centrifugation and washing by basic water (pH ∼ 8.5) for several times, the Pd$_{24}$L$_{48}$ cages confined in dendritic MSNs were reduced by sodium borohydride (NaBH$_4$) inducing the in situ MOC conversion into ultrasmall Pd nanoclusters (NCs).

The structure of Pd$_{24}$L$_{48}$ cage was first determined by nuclear magnetic resonance (NMR). As shown in the ^{1}H NMR spectrum (Figure 1B), the α and β protons on the pyridyl groups (H$_\alpha$ and H$_\beta$) are shifted downfield ($\Delta\sigma$ = 0.17 and 0.29 ppm for H$_\alpha$ and H$_\beta$, respectively) due to coordination to Pd^{2+}. Compared with pure ligand 1, the ^{1}H signals of the Pd$_{24}$L$_{48}$ cage are much broader. Moreover, the molecular weight of the Pd$_{24}$L$_{48}$ cage $\{[Pd_{24}(C_{22}H_{26}N_2S)_{48}]^{48+}\cdot 48\text{-}(NO_3^-)\}$ was calculated to be 22 338.99 Da, confirmed from the Pd$_{24}$L$_{48}$ compositions which displayed a series of prominent peaks for [Pd$_{24}$L$_{48}$ cage-(NO$_3^-$)$_m$]$^{m+}$ (m = 17, 24, 27, and 33, Figure 1C). Combined with the transmission electron microscopy (TEM) image in Figure 1D, which revealed the formation of ca. 4.3 nm diameter molecular nanoparticles, all of this information is consistent with the successful formation of the Pd$_{24}$L$_{48}$ cage.

As for the synthesized 3D-dendritic MSN, the TEM image in Figure S1 shows the highly uniform mesoporous nanosphere structure with a mean MSN diameter of ∼60 nm. The center-radial mesopore channel can also be clearly seen in the TEM image. From analysis of the N$_2$ adsorption−desorption isotherm (Figure 2B), the BET surface area of the 3D-dendritic MSN was determined to be ∼711.1 m^2 g^{-1}, and the total pore volume was found to be ∼1.57 cm^3 g^{-1}. Based on the Barrett−Joyner−Halenda (BJH) method, the pore size of the MSN was estimated to be about ca. 5.0 nm in diameter (Figure S2). Note that the large pore size around 23 nm can be attributed to the packing of the uniformly sized MSNs. FTIR was used to confirm the successful anchoring of the organosilanes, where the characteristic peaks assigned to the

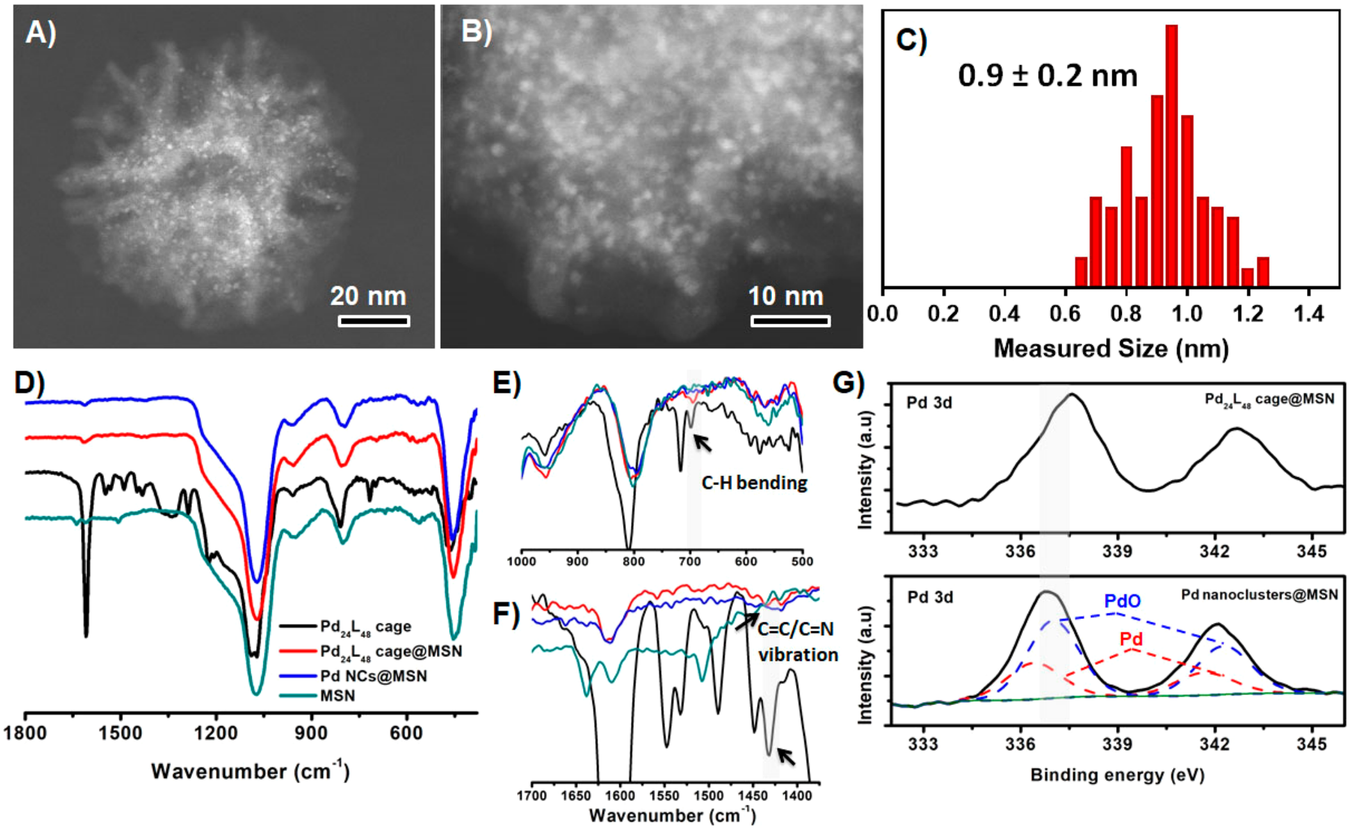

Figure 3. (A, B) STEM images of Pd NCs@MSN. (C) Histogram of the mean diameters of the confined Pd NCs ($N = 125$). (D−F) FTIR spectra of $Pd_{24}L_{48}$ cage, $Pd_{24}L_{48}$ cage@MSN, Pd NCs@MSN, and MSN. (G) High-resolution Pd 3d spectra of $Pd_{24}L_{48}$ cage@MSN (top), and Pd NCs@MSN (bottom); partial oxidation of some Pd nanoclusters has occurred due to air exposure.

organosilane and the functionalized MSN can be found in the region of 2800 and 3000 cm^{-1} (Figure S3). From single-crystal X-ray analysis,[27] the cage of $Pd_{24}L_{48}$ forms a rhombicuboctahedral structure that fits within a 3.6 nm diameter inscribed sphere. The distance between antipodal Pd−Pd atoms is 4.0 nm. The suitable MSN pore size suggests that the encapsulation of $Pd_{24}L_{48}$ cages within the mesopores can take place in a single-file fashion.

Due to the $Pd_{24}L_{48}$ cage solubility in DMSO, an easy wet-impregnation approach is applied for MOC incorporation into MSN. After loading, as shown in Figure 1E, the apparent 3D-dendritic MSN still maintains its original morphology. Owing to the relative sensitivity of MOC to electron beams or to a contrast issue, it was practically impossible to examine the $Pd_{24}L_{48}$ cages encapsulated within the pores by TEM imaging. Nevertheless, direct photographs clearly showed that the $Pd_{24}L_{48}$ cage@MSN was obtained as a yellow pellet (color of MOC solution) compared to the solid white color of bare MSNs, which is indicative of the successful encapsulation (Figure S4). Moreover, energy-dispersive X-ray (EDX) mapping analysis also confirms the presence of $Pd_{24}L_{48}$ cage in MSN, with a relatively homogeneous distribution of Pd within the silica framework (Figure 1G−I). Correspondingly, S_{BET} results show a decrease of the BET surface area of 3D-dendritic MSN from 711.1 to 540.4 $m^2\ g^{-1}$ (Figure 2B,C), along with a reduction in total pore volume from 1.57 to 1.22 $cm^3\ g^{-1}$. By using ICP-MS and N_2 sorption data, one particle is calculated to house approximately 460 $Pd_{24}L_{48}$ cages, which corresponds to about 40% surface coverage (detailed calculation in the Supporting Information). The successful loading of a large amount of MOCs in dendritic MSNs with nearly monolayer packing throughout the mesopore network provides an important prerequisite for later metal nanocluster formation.

The conversion of MOC into metal NCs was carried out by direct chemical reduction in aqueous $NaBH_4$ (Figure 2A). ζ potential analysis of the cage-free 3D-dendritic MSN suspensions at different pH values shows an isoelectric point (pI ∼ 6.1), which is the direct result of the incorporated thiol/aniline. The positively charged $Pd_{24}L_{48}$ cage (suspended in DMSO) loading within MSN pores is then dominated by a local electrostatic interaction with both silanolate ($\equiv SiO^-$) and thiolate ($—S^-$) groups inducing a significant shift of the pI to ca. 8.5 (Figure 2D). To enhance the surface interaction (electrostatic interactions) between the $Pd_{24}L_{48}$ cage and the silica pore surface, the $Pd_{24}L_{48}$ cage@MSN was incubated in pH 8.5 solution for several minutes, and then $NaBH_4$ aqueous solution was directly added to promote the reduction. After being washed for three times, the isolated pellet turns dark-brownish gray, visually indicating the successful reduction (Figure S4).

The cage encapsulated MSN shows a similar UV−vis absorption spectrum to that of a free cage suspension. However, after reduction, the prominent peaks (367 nm) attributed to the Pd^{2+}-coordinated organic ligand of $Pd_{24}L_{48}$ cage disappeared, and a broad shoulder around 340−390 nm appeared corresponding to the formation of Pd NCs, further confirming the generation of Pd NCs (Figure 2E).[38] Compared to $Pd_{24}L_{48}$ cage@MSN, which showed a considerable hydrodynamic size increase compared to bare MSNs as

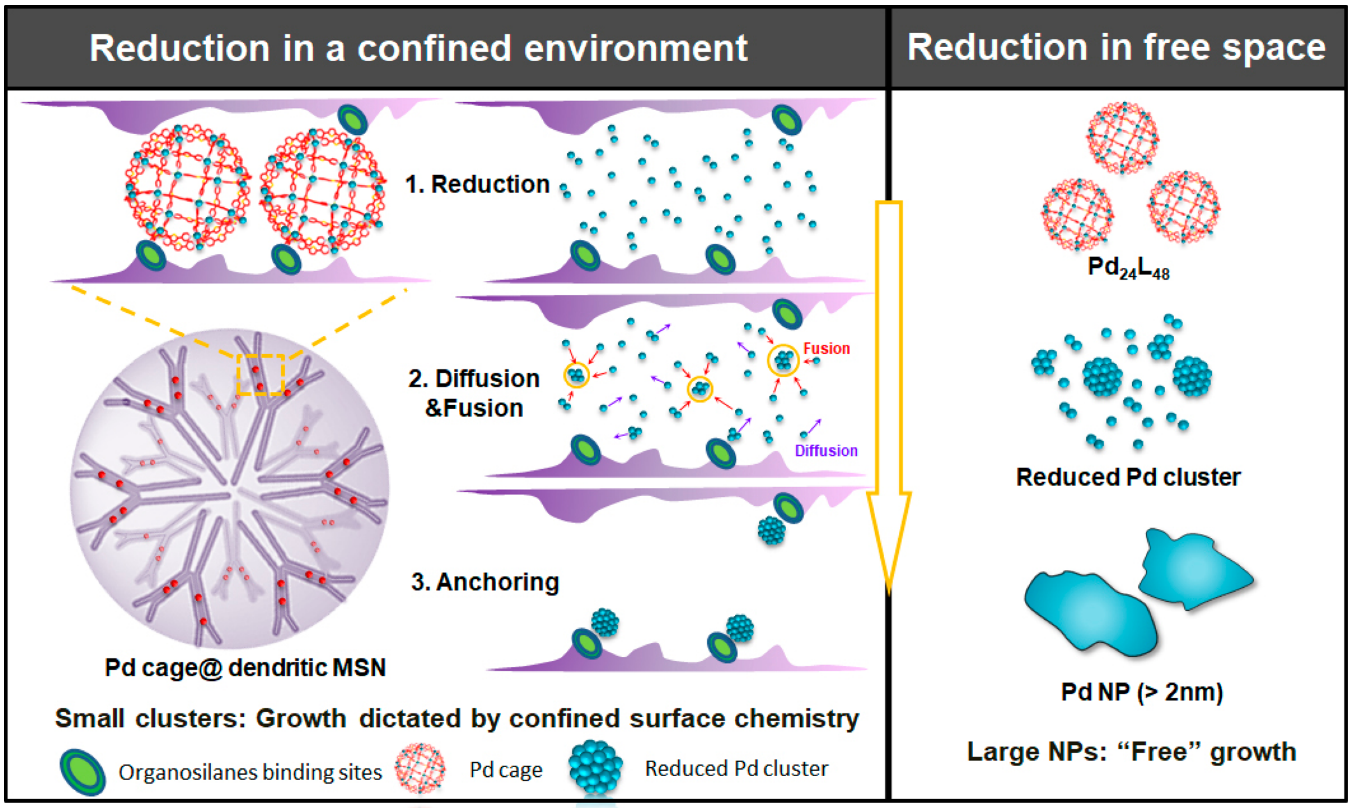

Figure 4. Schematic illustration of the formation mechanism of Pd NCs confined in MSN and the "free" growth of Pd NPs in solution.

well as some aggregation trends in water (shown by a relatively higher polydispersity index, PDI), the particles after MOC reduction exhibit smaller hydrodynamic size and an excellent dispersibility (Figure 2F), which is a key feature for any further catalytic study. Also S_{BET} analysis shows surface area recovery to 684.1 m^2 g^{-1} and pore volume recovery to 1.48 cm^3 g^{-1}. High-magnification high-angle annular dark-field scanning transmission electron microscopy (HAADF-STEM) images (Figure 3A,B) of the Pd NCs@MSN show a homogeneous dispersion of Pd NCs on the dendritic MSN surface with a mean particle diameter of 0.9 nm ± 0.2 nm (n = 125, Figure 3C). From ICP-MS analysis, the Pd concentration on MSNs before and after reduction was found to be 1.77 and 1.56 wt %, respectively, indicating most of Pd ions from MOC have been reduced and anchored on the MSN surface. Moreover, Fourier transform infrared spectrophotometry (FTIR) of $Pd_{24}L_{48}$ cage@MSN also proved the successful loading of cage inside MSN by the presence of the characteristic C=C/C=N vibration peak (1433 cm^{-1}) and C—H bending vibration peak (696 cm^{-1}) that corresponds to the thiophene group (Figure 3D−F). Note that, due to the effects of restricted vibrational motion (torsion, bending, etc.), some of the vibration peaks corresponding to the $Pd_{24}L_{48}$ cage disappeared compared to the free cage state. This confinement induced loss of vibrational peaks has also been observed by other researchers.[39−41] Nevertheless, after reduction, both of the characteristic peaks assigned to the cage disappeared, indicating the formation of ligand-free Pd NCs decorating the MSN surface. Compared to the solution phase synthesis of Pd NCs where an excess amount of organic capping agents such as alkyl thiol were added for protection, in our case the low amount of organic capping agents derived from cage reduction (Pd:organic ligand = 1:2 in molar ratio) is the main reason for the formation of ligand-free Pd NCs. Unlike alkyl groups with pending thiols that exhibit high binding affinity to the Pd surface, the ligand 1 used herein is sterically hindered by surrounding pyridines, which limits any further binding to formed Pd nanoclusters. These two factors promote the formation of ligand-free Pd NCs in our case. Additionally, X-ray photoelectron spectroscopy (XPS) analysis also proves the presence of Pd atoms. The Pd $3d_{5/2}$ peak was fitted by two peaks with binding energies of 336.4 and 337.0 eV, corresponding to the metallic Pd (0) and oxidized Pd, respectively. From XPS results, ca. 69% Pd (0) has been oxidized most likely due to the long-time air exposure during XPS sample preparation.[42] Nevertheless, all these results clearly confirmed the confined reduction of MOC into ligand-free metal NCs sheltered within silica mesopores.

To facilitate the understanding of the confined reduction process, the reduction of a conventional palladium source, H_2PdCl_4, in dendritic MSNs and the reduction of free, unconstrained $Pd_{24}L_{48}$ cages in solution were carried out. To enable comparison with the above-described MOC reduction confined within MSN, the Pd ion concentrations for both control samples and the corresponding amount of reducing agent have been adjusted to the same ratio. Nevertheless, after the same reduction process, only larger Pd nanocrystals (>2 nm) could be achieved (Figure S5A,B). Moreover, for a similar 3D-dendritic MSN morphology but with larger pore size (~12 nm), which enables more than one layer of MOC packing across the pore channel, reduction results in larger Pd nanocrystals ca. 3.2 nm in diameter (Figure S5C), emphasizing the importance of confined reduction. The metal nanocluster formation mechanism can be explained as shown in Figure 4.

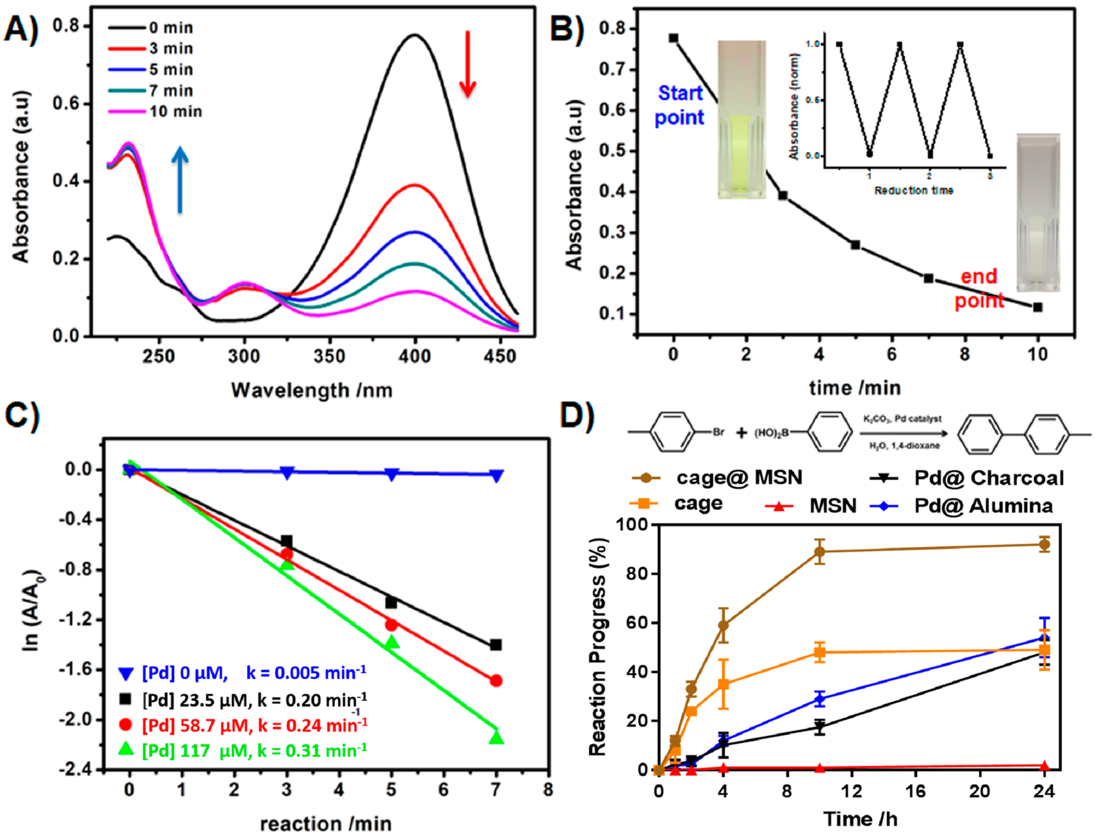

Figure 5. (A) UV–vis spectra of the reduction of 4-nitrophenol to 4-aminophenol with sodium borohydride catalyzed by Pd NCs@MSN. (B) Plots of normalized absorption intensity (400 nm) related to reaction time; insets are the optical image of 4-nitrophenol before and after reduction, and reduction of 4-nitrophenol at various runs in the recycle and reuse of Pd NCs@MSN. (C) Absorption intensity (400 nm) related to reaction time at different concentrations of Pd NCs@MSN, and pure MSN as control. (D) Suzuki–Miyaura coupling reaction and the associated catalytic performance of Pd NCs@MSN, free Pd nanocrystals, bare MSN, and commercial supported Pd catalysts overtime.

Due to the nearly identical diameters of MOC and silica mesopore channels, the MOC shows only single-file packing inside the pore channel resulting in a sub-monolayer. Moreover, the positive charge of MOC further increases the distance of cages from each through electrostatic repulsion, while maintaining the necessary interaction with silica walls through the organothiol-silane binding sites. Assuming all the metal ions belonging to MOC could be reduced at the same time to generate free Pd(0) atoms, due to the high surface energy and spatial distance, the free metal atoms belonging to the same cages tend to fuse into larger individual clusters. Although atom diffusion affects the growth of metal NCs, the atomic interdiffusions derived from different cages weaken the diffusion effect to a certain extent. Finally, through a reduction, diffusion, coalescence, and anchoring process in a confined space, UNMN formation through MOC conversion inside silica mesopores was achieved.

Herein, to highlight the catalytic activity of the Pd NCs@MSN, a reduction of 4-nitrophenol (4-NP) was carried out as a model reaction. The reduction of 4-NP was continuously monitored by UV–vis spectroscopy. As shown in Figure 5A, with the progress of reaction, the absorption peak of 4-NP at λ = 400 nm decreased quickly, accompanied by an increase of the absorption peak at λ = 232 nm, indicating the fast conversion of 4-NP to 4-aminophenol (Figure 5A). After conducting the reduction reaction for 10 min, the solution color changed from bright yellow to colorless (Figure 5B). As a control experiment, the Pd-free dendritic MSNs were also used for catalytic study under the same conditions. Reaction rates were calculated from plotting $\ln(A/A_0)$ versus reaction time, in which A_0 is the initial absorption intensity at λ = 400 nm, and A is the real-time absorption intensity at the same wavelength. The rate fitting was based on a first-order reaction model following reported work.[43] For bare MSN, negligible catalytic activity ($5.54 \times 10^{-3} \pm 2.77 \times 10^{-5}$ min^{-1}) was observed (Figure 5C). However, for Pd NCs@MSN with relatively low Pd concentration (2.35×10^{-5} mol L^{-1}), the reaction rate constant increased by 36-fold and was calculated to be $0.20 \pm 0.91 \times 10^{-3}$ min^{-1}. Moreover, the catalyst concentration-dependence of the reduction reaction was determined for a constant 4-NP concentration. Using the same fitting procedure, the calculated rate constants increased to $0.24 \pm 7.79 \times 10^{-3}$ and $0.31 \pm 2.11 \times 10^{-2}$ min^{-1}, when the Pd concentration was subjected to a 2.5- and 5-fold increase ([Pd] = 5.87×10^{-5} and 1.17×10^{-4} mol L^{-1}), respectively (Figure 5B). These rate increases proved the high catalytic activity of Pd NCs. Note that the varied concentration of Pd was attributed to the amount of NP (Pd NCs@MSN) in solution. Importantly, after each catalytic cycle, the Pd NCs@dendritic MSN catalyst could be recovered by simple centrifugation, followed by washing with water. The catalysts maintained a high activity even after three successive cycles of reactions (Figure 5B, inset).

We also tested the efficiency of Pd NCs@MSN in the Pd-catalyzed coupling of an organo boronic acid to a halide, known as the Suzuki–Miyaura reaction. We first carried out a control experiment with Pd-free MSNs, and expectedly, these bare MSNs showed no coupling even after 24 h of incubation (Figure 5D). We then performed 2 reactions with free (unconfined) reduced cages (Pd nanocrystals) and MSN-loaded reduced cages (Pd NCs@MSN). While the free reduced cage sample showed only 50% reaction after 24 h, the MSN-laden catalyst resulted in 90% reaction after 24 h. Additionally, the same reaction was carried out using commercial supported Pd catalysts, namely, Pd@alumina and Pd@activated charcoal, and as seen in Figure 5D, the reaction progress is significantly slower and reaches similar results as compared to the free cage (48−54% after 24 h). These results are clearly indicative of the importance of nanoconfinement and thiol-mediated surface attachment on MOC reduction and the catalytic activity of the resulting ligand-free NCs. The confined reduction of MOC within highly porous MSN allowed creating, *in situ*, ligand-free UNMN nanocatalyst with important catalytic activity that, compared to a free catalyst, is more powerful and reliable.

In conclusion, we were able to controllably produce sub-nm ligand-free UNMN nanocatalysts upon in situ reduction of MOC ($Pd_{24}L_{48}$) confined as an approximate monolayer within 3D-dendritic mesoporous silica nanoparticles. The presence of Pd NCs within the silica mesopores was detected and confirmed by UV, XPS, N_2 sorption, and STEM. The importance of the confined reduction was highlighted by control experiments using free MOC and other noncage Pd sources that both showed larger metal clusters. The dispersibility of Pd NCs within the mesopores and the stability of these new complex nanoconstructs in the loading and reduction conditions were key features that were harnessed to achieve small Pd NP size and high catalytic activity. Based on the confined reduction of MOC in MSN, ligand-free metal NCs with high catalytic activities were easily and efficiently achieved. Indeed, very good catalytic performances were shown for Pd NCs@MSN in the reduction of nitrophenol into aminophenol which exhibited very fast reaction kinetics and also for the C−C Suzuki−Miyaura coupling reaction compared to free cages and commercial supported Pd catalysts. These results confirm the accessibility, stability, and activity of the confined ligand-free Pd clusters “in situ anchored” on the silica mesopore surfaces following MOC reduction. Our overall approach of confined reductive transformation of MOCs into UNMNs should be translatable to the multitude of other possible cluster molecules and nanoporous support architectures where confinement and surface anchoring might also lead to greater thermal stability by suppressing thermal coarsening. We believe that our approach is robust and exhibits sufficient reliability and tunability to be translated into large-scale applied fields.

■ ASSOCIATED CONTENT

Ⓢ Supporting Information

The Supporting Information is available free of charge on the ACS Publications website at DOI: 10.1021/acs.nanolett.8b04121.

> Additional experimental details and figures including TEM images, pore distribution, FTIR spectra, and photographs (PDF)

■ AUTHOR INFORMATION

Corresponding Author

*E-mail: jbrinker@unm.edu.

ORCID

Achraf Noureddine: 0000-0001-9530-5963
C. Jeffrey Brinker: 0000-0002-7145-9324

Author Contributions

W.Z. and A.N. contributed equally. The manuscript was written through contributions of all authors. All authors have given approval to the final version of the manuscript.

Notes

The authors declare no competing financial interest.

■ ACKNOWLEDGMENTS

The authors acknowledge support by the Sandia National Laboratory Laboratory-Directed Research and Development Program and the US Department of Energy, Office of Science, Division of Catalysis Science program under Grant DE-FG02-02ER15368. This work was supported, in part, by the National Science Foundation under Cooperative Agreement EEC-1647722. Sandia National Laboratories (SNL) is a multi-mission laboratory managed and operated by National Technology and Engineering Solutions of Sandia, LLC, a wholly owned subsidiary of Honey-well International, Inc., for the U.S. Department of Energy’s National Nuclear Security Administration under Contract DENA-0003525. This paper describes objective technical results and analysis. Any subjective views or opinions that might be expressed in the paper do not necessarily represent the views of the U.S. Department of Energy or the United States Government.

■ REFERENCES

(1) Tao, Y.; Li, M.; Ren, J.; Qu, X. *Chem. Soc. Rev.* **2015**, *44*, 8636−8663.

(2) Fang, J.; Zhang, B.; Yao, Q.; Yang, Y.; Xie, J.; Yan, N. *Coord. Chem. Rev.* **2016**, *322*, 1−29.

(3) Zhang, L.; Wang, E. *Nano Today* **2014**, *9*, 132−157.

(4) Yu, Y.; Mok, B. Y. L.; Loh, X. J.; Tan, Y. N. *Adv. Healthcare Mater.* **2016**, *5*, 1844−1859.

(5) Wilcoxon, J. P.; Abrams, B. L. *Chem. Soc. Rev.* **2006**, *35*, 1162−1194.

(6) Jin, R.; Zeng, C.; Zhou, M.; Chen, Y. *Chem. Rev.* **2016**, *116*, 10346−10413.

(7) Jin, R. *Nanoscale* **2015**, *7*, 1549−1565.

(8) Wan, X.; Yuan, S.; Tang, Q.; Jiang, D.; Wang, Q. *Angew. Chem., Int. Ed.* **2015**, *54*, 5977−5980.

(9) Wang, Y.; Wan, X.; Ren, L.; Su, H.; Li, G.; Malola, S.; Lin, S.; Tang, Z.; Häkkinen, H.; Teo, B. K.; Wang, Q.; Zheng, N. *J. Am. Chem. Soc.* **2016**, *138*, 3278−3281.

(10) Yamamoto, K.; Imaoka, T.; Chun, W.; Enoki, O.; Katoh, H.; Takenaga, M.; Sonoi, A. *Nat. Chem.* **2009**, *1*, 397−402.

(11) Ye, H.; Crooks, R. M. *J. Am. Chem. Soc.* **2007**, *129*, 3627−3633.

(12) Argo, A. M.; Odzak, J. F.; Gates, B. C. *J. Am. Chem. Soc.* **2003**, *125*, 7107−7115.

(13) Kaden, W. E.; Wu, T.; Kunkel, W. A.; Anderson, S. L. *Science* **2009**, *326*, 826−829.

(14) Imaoka, T.; Kitazawa, H.; Chun, W.; Yamamoto, K. *Angew. Chem., Int. Ed.* **2015**, *54*, 9810−9815.

(15) Huang, W.; Kuhn, J. N.; Tsung, C.; Zhang, Y.; Habas, S. E.; Yang, P.; Somorjai, G. A. *Nano Lett.* **2008**, *8*, 2027−2034.

(16) Guo, Z.; Xiao, C.; Maligal-Ganesh, R. V.; Zhou, L.; Goh, T. W.; Li, X.; Tesfagaber, D.; Thiel, A.; Huang, W. *ACS Catal.* **2014**, *4*, 1340−1348.

(17) Yamazoe, S.; Kouasu, K.; Tsukuda, T. *Acc. Chem. Res.* **2014**, *47*, 816−824.

(18) Ye, R.; Zhukhovitskiy, A. V.; Deraedt, C. V.; Toste, F. D.; Somorjai, G. A. *Acc. Chem. Res.* **2017**, *50*, 1894−1901.

(19) Liu, B.; Yao, H.; Song, W.; Jin, L.; Mosa, I. M.; Rusling, J. F.; Suib, S. L.; He, J. *J. Am. Chem. Soc.* **2016**, *138*, 4718−4721.

(20) McConnell, A. J.; Wood, C. S.; Neelakandan, P. P.; Nitschke, J. R. *Chem. Rev.* **2015**, *115*, 7729−7793.

(21) Yan, X.; Cook, T. R.; Wang, P.; Huang, F.; Stang, P. J. *Nat. Chem.* **2015**, *7* (22), 342−348.

(22) Sun, Q. F.; Sato, S.; Fujita, M. *Nat. Chem.* **2012**, *4*, 330−333.

(23) He, C.; Lin, Z.; He, Z.; Duan, C.; Xu, C.; Wang, Z.; Yan, C. *Angew. Chem., Int. Ed.* **2008**, *47*, 877−881.

(24) Cao, A.; Zhu, W.; Shang, J.; Klootwijk, J. H.; Sudhölter, E. J. R.; Huskens, J.; de Smet, L. C. P. M. *Nano Lett.* **2017**, *17*, 1−7.

(25) Sun, L.; Li, J.; Lu, W.; Gu, Z.; Luo, Z.; Zhou, H. *J. Am. Chem. Soc.* **2012**, *134*, 15923−15928.

(26) Kang, Y.; Liu, X.; Yan, N.; Jiang, Y.; Liu, X.; Sun, L.; Li, J. *J. Am. Chem. Soc.* **2016**, *138*, 6099−6102.

(27) Sun, Q.; Iwasa, J.; Ogawa, D.; Ishido, Y.; Sato, S.; Ozeki, T.; Sei, Y.; Yamaguchi, K.; Fujita, M. *Science* **2010**, *328*, 1144−1147.

(28) Fujita, D.; Ueda, Y.; Sato, S.; Mizuno, N.; Kumasaka, T.; Fujita, M. *Nature* **2016**, *540*, 563−566.

(29) Zarra, S.; Wood, D. M.; Roberts, D. A.; Nitschke, J. R. *Chem. Soc. Rev.* **2015**, *44*, 419−432.

(30) Li, J.-R.; Yakovenko, A. A.; Lu, W.; Timmons, D. J.; Zhuang, W.; Yuan, D.; Zhou, H.-C. *J. Am. Chem. Soc.* **2010**, *132* (49), 17599−17610.

(31) Li, J.-R.; Yu, J.; Lu, W.; Sun, L.-B.; Sculley, J.; Balbuena, P. B.; Zhou, H.-C. *Nat. Commun.* **2013**, *4*, 1538.

(32) Osuga, T.; Murase, T.; Hoshino, M.; Fujita, M. *Angew. Chem., Int. Ed.* **2014**, *53*, 11186−11189.

(33) Qiao, J.; Shi, K.; Wang, Q. *Angew. Chem., Int. Ed.* **2010**, *49*, 1765−1767.

(34) Harris, K.; Fujita, D.; Fujita, M. *Chem. Commun.* **2013**, *49*, 6703−6712.

(35) Takao, K.; Suzuki, K.; Ichijo, T.; Sato, S.; Asakura, H.; Teramura, K.; Kato, K.; Ohba, T.; Norita, T.; Fujita, M. *Angew. Chem., Int. Ed.* **2012**, *51*, 5893−5896.

(36) Shen, D.; Yang, J.; Li, X.; Zhou, L.; Zhang, R.; Li, W.; Chen, L.; Wang, R.; Zhang, F.; Zhao, D. *Nano Lett.* **2014**, *14*, 923.

(37) Durfee, P. N.; Lin, Y.; Dunphy, D. R.; Muñiz, A. J.; Butler, K. S.; Humphrey, K. R.; Lokke, A. J.; Agola, J. O.; Chou, S. S.; Chen, I.; Wharton, W.; Townson, J. L.; Willman, C. L.; Brinker, C. J. *ACS Nano* **2016**, *10*, 8325−8345.

(38) Gaikwad, A. V.; Rothenberg, G. *Phys. Chem. Chem. Phys.* **2006**, *8*, 3669−3675.

(39) Wang, C.; Shang, J.; Lan, Y.; Tian, T.; Wang, H.; Chen, X.; Gu, J.; Liu, J.; Wan, L.; Zhu, W.; Li, G. *Adv. Funct. Mater.* **2015**, *25*, 6009−6017.

(40) Hashimoto, S.; Fujimori, T.; Tanaka, H. *J. Am. Chem. Soc.* **2011**, *133*, 2022−2024.

(41) Marchese, L.; Frache, A.; Gianotti, E.; Martra, G.; Causà, M.; Coluccia, S. *Microporous Mesoporous Mater.* **1999**, *30*, 145−153.

(42) Wu, P.; Huang, Y.; Kang, L.; Wu, M.; Wang, Y. *Sci. Rep.* **2015**, *5*, 14173−14181.

(43) Wunder, S.; Lu, Y.; Albrecht, M.; Ballauff, M. *ACS Catal.* **2011**, *1*, 908−916.